



Numerical Study of the Aerodynamic Performance of a Train with a Crosswind for Different Embankment Heights

Xianli Li^{1,2,3,4} · Guang Chen^{1,2,3} · Siniša Krajnović⁵ · Dan Zhou^{1,2,3}

Received: 19 February 2020 / Accepted: 23 August 2020 / Published online: 1 September 2020
© Springer Nature B.V. 2020

Abstract

A numerical study using improved delayed detached eddy simulation (IDDES) was used to investigate the influence of the embankment height on the aerodynamic performance of a high-speed train travelling under the influence of a crosswind. The results of the flow predictions were used to explore both the instantaneous and the time-averaged flows and the resulting aerodynamic forces, moments and slipstreams. An increase of the aerodynamic drag and side forces as well as the lift force of the head and middle cars were observed with rising embankment height. While the lift force of the tail car decreased with the increasing embankment height. Furthermore, the height of the embankment was found to have a strong influence on the slipstream on the leeward side of the train. The correlation between the embankment height and the slipstream velocity on the windward side, was rather small. The flow structures in the near-wake of the leeward side of the train, responsible for the aerodynamic properties of the train were analyzed, showing strong dependency on the embankment height.

Keywords IDDES · Embankment · Crosswind · Slipstream · Flow structures

✉ Dan Zhou
zd_lzj@126.com

¹ Key Laboratory of Traffic Safety on Track (Central South University), Ministry of Education, Hunan 410075 Changsha, People's Republic of China

² Joint International Research Laboratory of Key Technology for Rail Traffic Safety, Hunan 410075 Changsha, People's Republic of China

³ School of Traffic and Transportation Engineering, Central South University, Hunan 410075 Changsha, People's Republic of China

⁴ School of Civil Engineering, Central South University, Hunan 410075 Changsha, People's Republic of China

⁵ Department of Mechanics and Maritime Sciences, Chalmers University of Technology, 41296 Gothenburg, Sweden

1 Introduction

A train operating in the open air forms a slipstream as a result of the air displacement around the train. The turbulent flow in the region near the train sides is moving at the speed comparable to that of the train leading to safety risks for objects, people and animals close to the train. The problem with slipstream has increased with high-speed trains (HSTs) operating at speeds of 300 km/h and higher. A number of incidents caused by slipstream have been reported in UK, Switzerland, and Austria (Pope 2006; Flynn et al. 2016; Chen et al. 2019a), leading to a need for a research of the phenomena and how to prevent it.

Several studies of the slipstreams of trains have been performed in the absence of crosswinds. For example, Wang et al. (2018a) compared the effects of the presence or absence of bogies on the slipstream around a train. Xia et al. (2017) compared the effects of stationary and moving ground on the slipstream and the wake flows around a train using numerical simulations. Flynn et al. (2014) used the detached eddy simulation (DES) method to study the time-averaged and instantaneous slipstream around a freight train. During their operation, HSTs are often exposed to crosswinds influencing their aerodynamic performance. In particular, safety implications of the crosswinds on HSTs have led to several experimental and numerical studies. Cheli et al. (2010a) made wind tunnel tests to compare the differences in the aerodynamics for original and optimized cars. Krajnović et al. (2012) used large eddy simulation (LES) method to study the differences in the aerodynamic performances for static and moving trains during crosswind conditions. They found significant differences in the aerodynamic performances of static and moving trains. In particular, the difference in the yawing angle moment was reported to more than 30%. Munoz-Paniagua et al. (2017) compared the accuracy of different turbulence models (Reynolds-Averaged Navier–Stokes (RANS), scale-adaptive simulation (SAS), and improved delayed detached eddy simulation (IDDES) for predicting the aerodynamic performance of a train during crosswind conditions. However, these studies mainly focused on the aerodynamic forces, the aerodynamic moments, the pressures on the train surfaces, and the vortices on the windward sides with crosswinds. A small number of studies focusing on slipstream around trains in crosswinds have shown that a slipstream with a crosswind is significantly different from that without a crosswind (Flynn et al. 2016; Chen et al. 2019a), and even at a yaw angle of less than $\pm 1.5^\circ$, the slipstream velocity will increase significantly at low wind speeds (Baker et al. 2014a, b). As a result, the slipstream around a train cannot be neglected when crosswinds are present.

Although the above-mentioned studies examined the slipstreams of trains with and without crosswinds, the influence of the embankment was neglected. Embankments are common structures along a railway line, as indicated in Fig. 1. A train on an embankment will be subjected to higher aerodynamics forces and moments during a crosswind compared to flat ground (Noguchi et al. 2019; Guo et al. 2020). Consequently, this poses greater safety risks (Tomasini et al. 2014). To ensure the safety of train operation on embankments during crosswinds, several studies have focused on the effects of embankments on the aerodynamic performances of trains. The influence of an embankment height change on the aerodynamic performance of a train during crosswind conditions was studied by Suzuki et al. (2003) and Cheli et al. (2010b) used wind tunnel tests to study the lift force and overturning moment of a train on the windward and leeward sides of a 6-m high embankment at different yaw angles. Tomasini et al. (2014) used wind tunnel tests to analyze the influences of embankments with different end layouts on train aerodynamic-force coefficients. Schober et al. (2010) compared the effects of different ground configurations on



Fig. 1 The embankment along a railway line

the aerodynamic performance of a train, including flat ground, flat ground with a ballast and rail, and a 6-m embankment. The results showed that different ground configurations had large influence on the aerodynamic performance of the train. Additional studies of the influence of embankments on the aerodynamic performances of trains is presented in Die-drichs et al. (2007) and Bocciolone et al. (2018). The studies mentioned above found that the different embankment models had large influence on the aerodynamic performances of trains. However, the studies only included the effects of embankment changes on the train aerodynamic forces, moments, and pressures. Influence of embankments on slipstreams was not included.

An example of a study where the influence of embankments on slipstreams was considered was that by Morden (2016) who studied the effect of embankment height on a slipstream with no crosswind. The results showed that the slipstream velocities of different embankment heights were significantly different around a train, especially in the near wake region. However, there are few studies of the influence of the embankment on the slipstream when the train is influenced by a crosswind. As a result of a crosswind on an embankment, the upstream flow is accelerated, resulting in a so called speed-up effect. This is closely related to the geometry model of an embankment (Zhang et al. 2019). Therefore, in this paper we studied the impact of the speed-up effect of different embankment heights on the slipstream around a train. Results of previous experimental and numerical studies Baker et al. (2014a, b), Baker (2010), Muld et al. (2012), Bell et al. (2014, 2016, 2017) showed the existence of two strong peaks in the slipstream velocity around the train. The present paper aims to explore the flow around the train that is responsible for the strength and the character of these.

2 Methodology

2.1 Geometry Model

In this study, a Deutsche Bahn Inter-City-Express 3 (ICE3) high-speed train model, previously used for aerodynamic studies of trains, was chosen as a train model. Its computer-aided design (CAD) model is freely available from the DIN Standards Railway Committee (FSF) (2018), as indicated in Fig. 2. The height (H) and width (W) of the train were 3.89 and 2.95 m, respectively, and the cross-sectional area was 10m^2 , as shown in Fig. 2a. The train height was chosen as the characteristic length scale. The train model consists of three

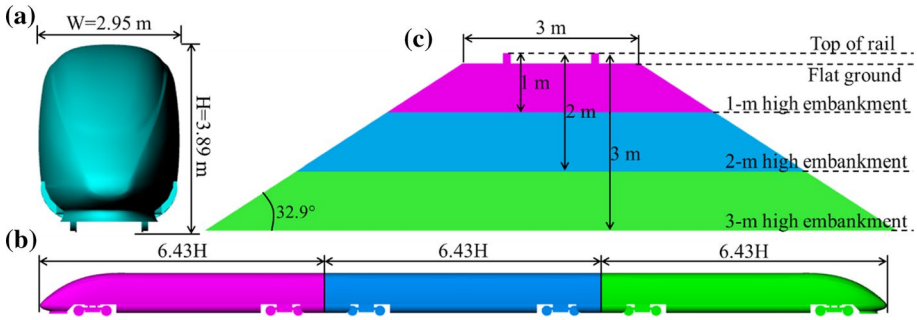


Fig. 2 Geometry models: **a** front view of the train; **b** side view of the train and **c** simplified model of different embankment heights and flat ground (FG)

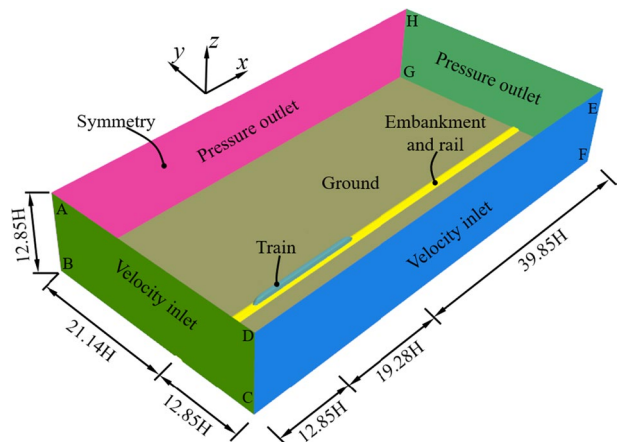
coaches, the head, middle, and tail cars, and the bogies were smoothed along the train’s surface, as shown in Fig. 2b. The lengths of the head, middle, and tail cars were $6.43h$, and the total length (L) of the train was $19.28H$.

Figure 2c shows the flat ground (the FG was considered to be an embankment with a height of $0m$ in this study) and the simplified model of different embankment heights. The embankment height was varied while keeping the angle of the beveled edge and the length of the top edge constant. The width of the top edge of the embankment was $3m$, and the angle between the beveled edge of the embankment and the horizontal plane was 32.9° . The length of the bottom edge was $5.55m$, 8.64 and $11.73m$ for embankment heights of $1m$, 2 and $3m$, respectively.

2.2 Computational Domain and Boundary Conditions

Figure 3 shows the computational domain and its boundary conditions. The length, width, and height of the computational domain were $71.98H$, $33.99H$, and $12.85H$, respectively. The coordinate system origin was located at the top of the rail (TOR) below the nose tip of the head car. The distance between the ABCD face and the nose tip of the head car was $12.85H$. The distance between the DCEF face and the plane $y=0$ was $12.85H$. To ensure

Fig. 3 Computational domain and boundary conditions



the full development of the flow field in the wake and on the leeward side of the train, the distance between the EFGH face and the nose tip of the tail car was $39.85H$, and the distance between the ABGH face and the plane $y=0$ was $21.14H$.

A steady uniform velocity profile was applied to the ABCD and DCEF faces. The resulting inlet velocity U_∞ of 60 m/s is shown in Fig. 4. The yaw angle β was 15° . The ABGF and EFGH faces were treated as pressure outlets, and the reference pressure P_∞ was 0 Pa. The ground, the rail, and the embankment had no-slip moving wall boundary conditions. A symmetric boundary condition was applied on the top surface of the computational domain. The Reynolds number (Re) was 1.53×10^6 based on the train height, H , and the train speed, u_{train} .

2.3 Numerical Method

The IDDES method (based on $k-\omega$ shear-stress transport) was used to study the flow field structure around the HST in this study. The IDDES method, which was proposed by Shur et al. (2008), combines the advantages of delayed detached-eddy simulation (DDES) with an improved RANS–LES hybrid model for wall modeling in the LES (WMLES) method. Similar to the classic DES blending technique, the IDDES method also uses a Reynolds-Averaged Navier–Stokes (RANS) model in the attached boundary layer and the LES model away from the boundary layers. For the traditional DES method, there are two main issues: grid-induced separation and log layer mismatch (Luckhurst et al. 2019). The former issue occurs because high grid resolution near a wall may cause the RANS region to enter the LES region prematurely. The latter issue occurs because the intercept of the log law region at the interface of the RANS and LES regions do not match. The IDDES method is designed to avoid these two problems in the traditional DES. Further information on this topic has been presented by Shur et al. (2008).

First, the flow field was initialized using the steady RANS simulation based on the shear-stress transport RANS (SST–RANS) model, and the obtained results were used in time-dependent simulations with the IDDES method. For the latter, the implicit-unsteady segregated incompressible finite-volume solver was selected in this study. The convection term used a hybrid bounded-central differencing scheme (hybrid-BCDS) and a hybrid second-order upwind scheme. The temporal discretization was second-order. The physical time step was fixed at $0.031t^*$ ($t^* = H/U_\infty$), each time step was iterated 30 times, and the total number of time steps was 20,000, corresponding to 4 s of simulation. A residual of 10^{-4} was achieved for each turbulence equation in each time step. All of the cases were calculated using STAR-CCM+ at the National Supercomputing Center (Wuxi, China).

Fig. 4 3D resultant velocity vector

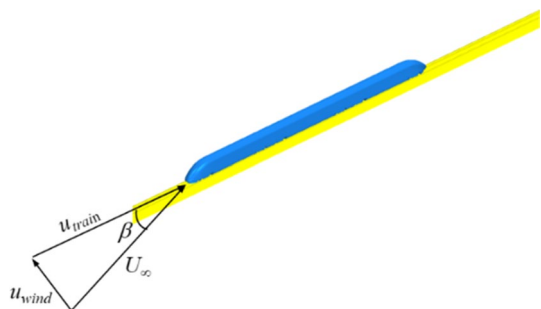
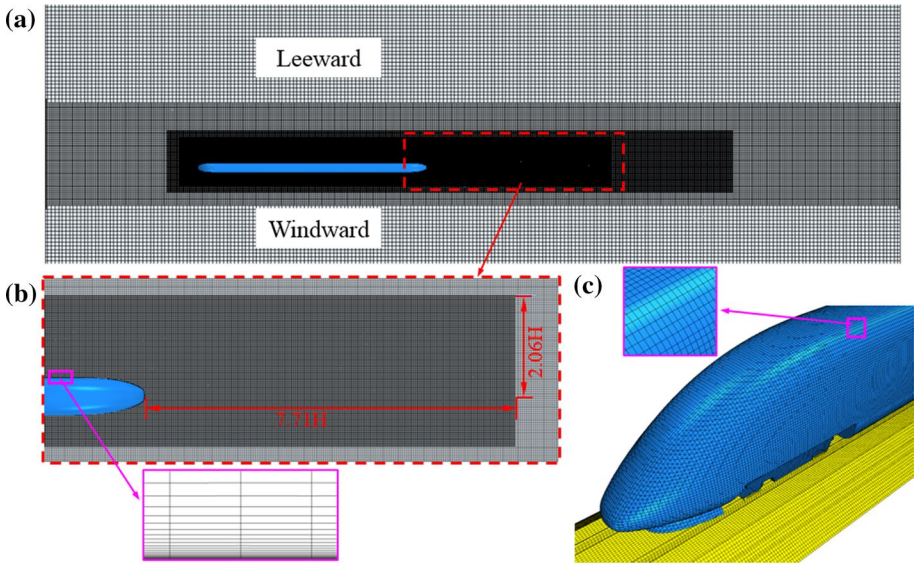


Table 1 Maximum spatial resolutions for coarse, medium, and fine meshes

Mesh	y^+	z^+	x^+	Number of cells/ $\times 10^6$
Coarse	3.5	960	960	15
Medium	0.95	480	480	30
Fine	0.95	240	240	50

**Fig. 5** Computational mesh: **a** plane at $z=1.04H$, **b** mesh at wake and prism-layer, and **c** mesh of train surface

2.4 Numerical Resolution

A mixed mesh was utilized in the computational domain, where a prism-layer mesh was used close to the train surface and a hexahedral mesh was used in the rest of the computational domain. A trimming technique was used to connect these two mesh types. To verify the mesh independence, three computational meshes, a coarse, a medium, and a fine meshes, containing 15 million, 30 million, and 50 million cells, respectively, were used. Table 1 shows the maximum spatial resolutions of the train surface cells expressed in wall units for all the results, for which y^+ is the dimensionless wall-normal distances between the trains' surface and the first computational node near the surface and z^+ and x^+ are dimensionless distances between the computational nodes in the streamwise and the spanwise directions, respectively. The Courant number was below 1 in 99% of the computational cells during entire computational time. Figure 5 shows the distribution of the medium mesh around a train. There were three local refinement boxes around the train. A mesh box close to the train surface was constructed to allow the resolution of the small-scale structures on the leeward side and in the wake of the train. The width of this box on the leeward side was $2.06H$, and the distance from the end of the box to the nose tip of the

tail car was $7.71H$. There were 20 prism-layers near the train surface with a growth rate of 1.15.

According to Flynn et al. (2016) and Bell et al. (2014), the slipstream velocity was defined as follows:

$$U = \frac{\sqrt{(u - u_{train})^2 + v^2}}{u_{train}}, \tag{1}$$

where u and v are the longitudinal and lateral velocity components in the computational domain, respectively, and u_{train} is the train velocity. Figure 6 shows the time-averaged pressure coefficients, defined in EN (2018), for the train surface and the slipstream velocity that were calculated using Eq. (1) at $y=0.77H$ and $z=0.36H$. The differences in the pressure coefficients for the three sets of grids on the upper train surface were found to be small, as shown in Fig. 6a, and there was only a small difference in the local region, as shown in the local magnification figure. The difference in the pressure coefficient between the medium and fine mesh was found to be less than 5%. Figure 6b shows the time-averaged slipstream velocity of the three sets of grids at $y=0.77H$ and $z=0.36H$. Also here, the difference in the velocity between the medium and fine meshes was found to be lower than 5%. The coarse mesh results were significantly different from those of the other meshes, especially in the positions of $6.2 < X/H < 14.3$ and $X/H > 20$. Thus, the mesh refinement study resulted in the choice of the medium mesh for the further investigation in the paper.

2.5 Validation Against the Experimental Data

A direct validation of the slipstream results of the present study was not possible due to the absence of the experimental data. This is often the case for the experimental data at large yaw angles and the validation is normally performed using indirect methods. Flynn et al. (2016) used the train surface pressure data obtained by wind tunnel tests to validate the accuracy of their numerical simulation when studying a slipstream during a crosswind. Similar validation was made by Chen et al. (2019a) who investigated the effects of different nose lengths on a slipstream during crosswinds. In this study, to validate the reliability of the numerical simulation, the side and lift forces of the numerical simulation of the FG and the single-track ballast and rail (STBR) were compared with the wind tunnel test results based on EN (2018).

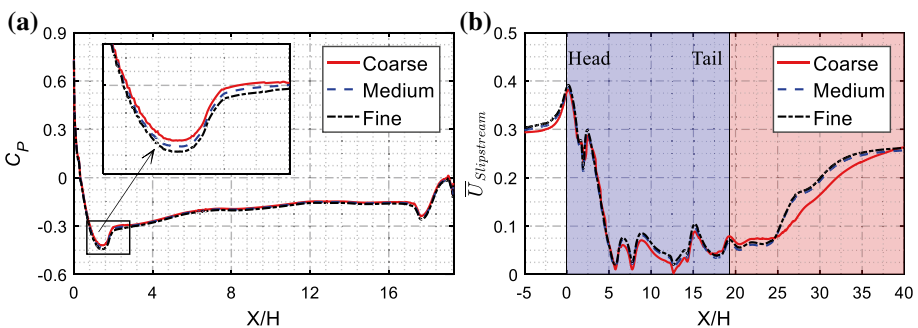


Fig. 6 Comparison of **a** the time-averaged pressures coefficients for the train surface and **b** the time-averaged slipstream velocities at $y=0.77H$ and $z=0.36H$ for the three sets of computational meshes

For the purpose of validation against the experimental data, an additional computation using stationary ground (including embankment and the rails) was performed. All other settings, such as the numerical method, boundary conditions, and mesh strategy, were unchanged. To facilitate the analysis, the aerodynamic force and moment were made dimensionless. Based on EN (2018), the drag, side force, lift force, and rolling moment coefficients were defined as follows:

$$C_d = \frac{F_d}{0.5\rho U_\infty^2 S}; \quad C_s = \frac{F_s}{0.5\rho U_\infty^2 S}; \quad C_l = \frac{F_l}{0.5\rho U_\infty^2 S}; \quad C_{mx} = \frac{M_x}{0.5\rho U_\infty^2 S d_0}, \quad (2)$$

where C_d , C_s , C_l , and C_{mx} represent the drag, side force, lift force, and rolling moment coefficients, respectively. F_d , F_s , F_l , and M_x represent the drag, side force, lift force, and rolling moment, respectively. The air density, ρ , was equal to 1.225 kg/m^3 . The free-stream velocity, U_∞ , was set to 60 m/s . The reference area, S , was set to 0.1 m^2 (a 1/10th scale ICE3 HST model was used), and the reference length, d_0 , according to the EN, was equal to 0.3 m .

The comparison of the side and lift force coefficients for the numerical simulation and the experiment is shown in Fig. 7. Figure 7a shows the comparison of the side and lift force coefficients of the FG. Figure 7b shows the comparison of the side and lift force coefficients of the STBR. The comparison showed that the difference in the lift force coefficients for the numerical prediction and the experiments was larger than that for the side force coefficients. However, the differences between the values predicted using the IDDES and the experimental data for the FG and STBR were only 6.3% and 5.7%, respectively. These differences could be explained with the differences in the geometric representations of the underbody of the train (e.g., bogie representation). These geometric differences may have resulted in differences in the underbody flow, resulting in a large difference in the lift force. Furthermore, the deviations of the numerically predicted side force coefficients for the experimental data for the FG and STBR were found to be less than 5%.

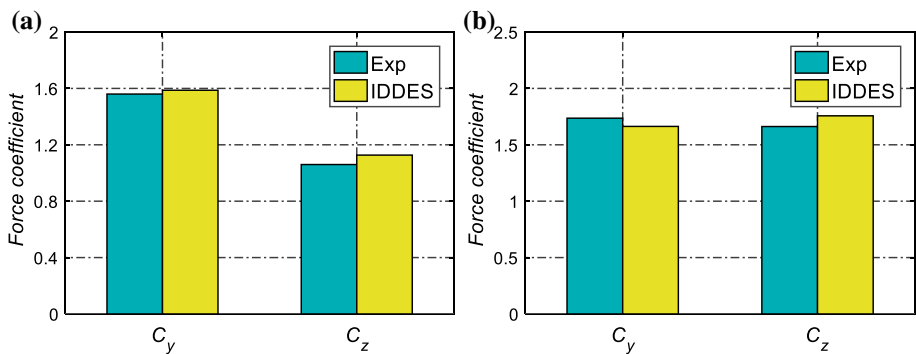


Fig. 7 Comparison of the side and lift force coefficients of the head car for the numerical simulation and experimental results: **a** FG and **b** STBR

Fig. 8 Measurement points of the slipstream velocity

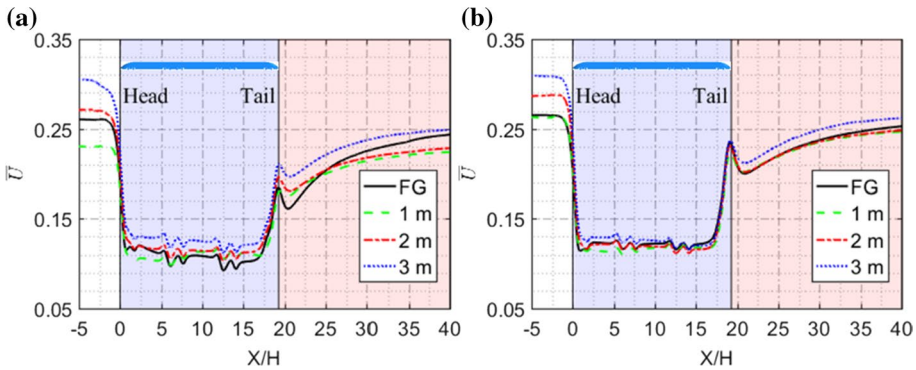
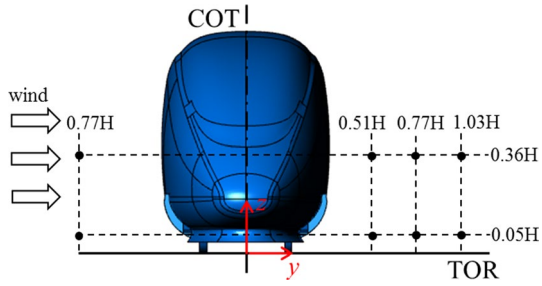


Fig. 9 Time-averaged slipstream velocity on the WS of the train at $y = -0.77H$ for a $z=0.05H$, and b $z=0.36H$

3 Results and Analysis

As described in this section, the numerical simulation results for different embankment heights, including the time-averaged slipstream velocity, instantaneous slipstream velocity, flow structures, and time-averaged aerodynamic force and moment coefficients were analyzed and compared. The time-averaged flow was initiated after time $154t^*$, once the flow was fully developed and stabilized (Hemida and Krajnović 2010). The instantaneous flow was analyzed at time $617t^*$.

3.1 Time-Averaged Slipstream Velocity

Figure 8 shows a schematic diagram of the position of the measurement points around the train. There were only two measurement points on the windward side (WS). Their heights from the top of rail (TOR) were $0.05H$, and $0.36H$, and the distance from the center of track (COT) was $0.77H$. There were six measurement points on the leeward side (LS). Their heights from the top of rail (TOR) were $0.05H$, and $0.36H$, and the distances from the center of track (COT) were $0.51H$, $0.77H$, and $1.03H$.

The time-averaged slipstream velocities on the WS of the train at $y = -0.77H$ for $z = 0.05H$ and $z = 0.36H$ are shown in Fig. 9. The variations of \bar{U} for the different embankment heights at $z = 0.05H$ and $z = 0.36H$ were similar. The velocity \bar{U} in the upstream region

was found to depend on the embankment heights, and whether $z=0.05H$ or $z=0.36H$. The highest \bar{U} was found for the 3 m embankment. In the nose region of the train, \bar{U} was found to decrease rapidly for both $z=0.05H$ and $z=0.36H$. Further downstream, in the boundary layer region, \bar{U} had rather constant value with fluctuation in the regions of the bogies. In the near wake region, the value of \bar{U} increased rapidly, resulting in a peak value at the tail of the train. In the far wake region, \bar{U} was found to converge to a constant value. The underlying reasons for such a distribution of \bar{U} are discussed in Sect. 3.3.1.

Figure 10 shows \bar{U} at different measurement points on the LS. Compared with the WS, the U on the LS was found to be more turbulent, especially the \bar{U} value at $y=0.51H$ and $z=0.36H$, which was due to the acceleration effect of the bogie. The value of the \bar{U} was found to increase in the region around the bogie. For the other measurement points, the peak value of \bar{U} is in the nose region. This position of the peak value of \bar{U} is different from the situation without crosswind, where the peak value of \bar{U} is normally observed in the near wake region (Wang et al. 2017; Chen et al. 2019b).

The \bar{U} peak values of different measurement points in the nose region decreased continuously with the increasing distance from the COT. Moreover, at $z=0.36H$, the position of the measurement point increased from $y=0.51H$ to $y=0.77H$, and the peak value of

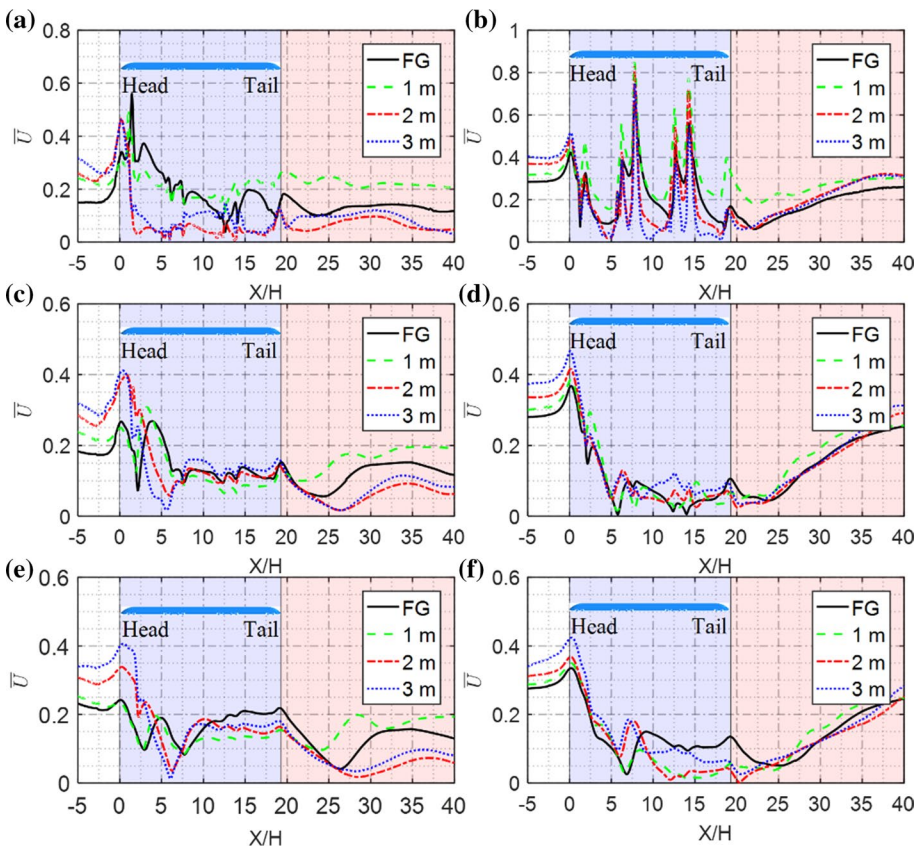


Fig. 10 Time-averaged slipstream velocity on the leeward side (left: $z=0.05H$, right: $z=0.36H$) **a**, **b** $y=0.51H$, **c**, **d** $y=0.77H$, and **e**, **f** $y=1.03H$

\bar{U} caused by the impact of the bogie completely disappeared, indicating that the effect of the bogie on the \bar{U} peak value was relatively small. By comparing the \bar{U} values at the different measurement points, as shown in Fig. 8, it could be determined that the peak value of \bar{U} in the nose region for a 3 m high embankment was the largest, and the difference between the \bar{U} peak value of the 1 m high embankment and the FG was found to be relatively small. When the embankment height increased from 0 to 3 m, the peak value of \bar{U} increased by 53.4% and 26.6% at $y=0.77H$, $z=0.05H$ and $y=0.77H$, $z=0.36H$, respectively. In the boundary layer region, the peak value of \bar{U} was similar to the relatively low \bar{U} value in the flow without crosswinds. Furthermore, because of the different heights of the embankment, the \bar{U} value was significantly different. In the near wake region, the \bar{U} value for the 1 m embankment height at different measurement points was larger than the values for the other embankment heights.

3.2 Gust Analysis

The variation in the embankment height was found to have small influence on the instantaneous U on the WS. Consequently, as described in this section, only the instantaneous U on the LS of the train at $y=0.77H$, $z=0.05H$, and $y=0.77H$, $z=0.36H$ were considered. The locations of the measurement points are shown in Fig. 8. According to the TSI specifications (European Union Agency for Railways 2014), the position of each measuring point required at least 20 individual runs. Therefore, measurements for 20 individual runs were obtained at $z=0.05H$ and $z=0.36H$ for each case. The *Moving Probe technique*, previously applied by Wang et al. (2017, 2018b) was used in this study to study the gust slipstream velocity around a train. The time interval between the two adjacent probes was $5.3t^*$ for the same measurement point position, and the movement speed was equal to the train speed, i.e., 57.96 m/s. Furthermore, the recording time with each probe had to be sufficiently long to capture the entire flow disturbance. To obtain the characteristic velocity, $U_{2\sigma}$, specified by TSI, a 1 s moving average (MA) was used for the raw data. The characteristic velocity was the maximum value of the average of 1 s MA plus two times the maximum value of the standard deviation after the 1 s MA, calculated as follows:

$$U_{2\sigma} = \bar{U}_p + 2\sigma \quad (3)$$

where \bar{U}_p is the maximum value of the average of the 1 s MA and σ is the maximum value of the standard deviation (SD) after 1 s MA.

Figure 11 shows the instantaneous U and 1 s MA on the LS at $z=0.05H$ and $z=0.36H$. The plots in the top row of Fig. 11a show the raw data (blue line), the ensemble average (black line), and the ensemble average plus two times the SD (red dashed line) at the measurement point at the track-side position. The plots in the lower row of Fig. 11a show 1 s MA of 20 individual probes (blue line), the ensemble average of 1 s MA (black line), and the ensemble average of 1 s MA plus two times the standard deviation (red dashed line) at the measurement point at $z=0.05H$. Figure 11b is similar to Fig. 11a and it shows the instantaneous U and 1 s MA at $z=0.36H$. Unlike the instantaneous U of a high-speed train without a crosswind (Baker 2010; Bell et al. 2014), the peak value of the ensemble average appeared near the head car and not in the near wake region under crosswind conditions. Furthermore, the difference in the ensemble average was significant for the different embankment heights, including the raw data and 1 s MA. The maximum value of the ensemble average of the raw data and 1 s MA increased with the increasing embankment height. When the embankment height increased from 0 to 3 m, the maximum value of the

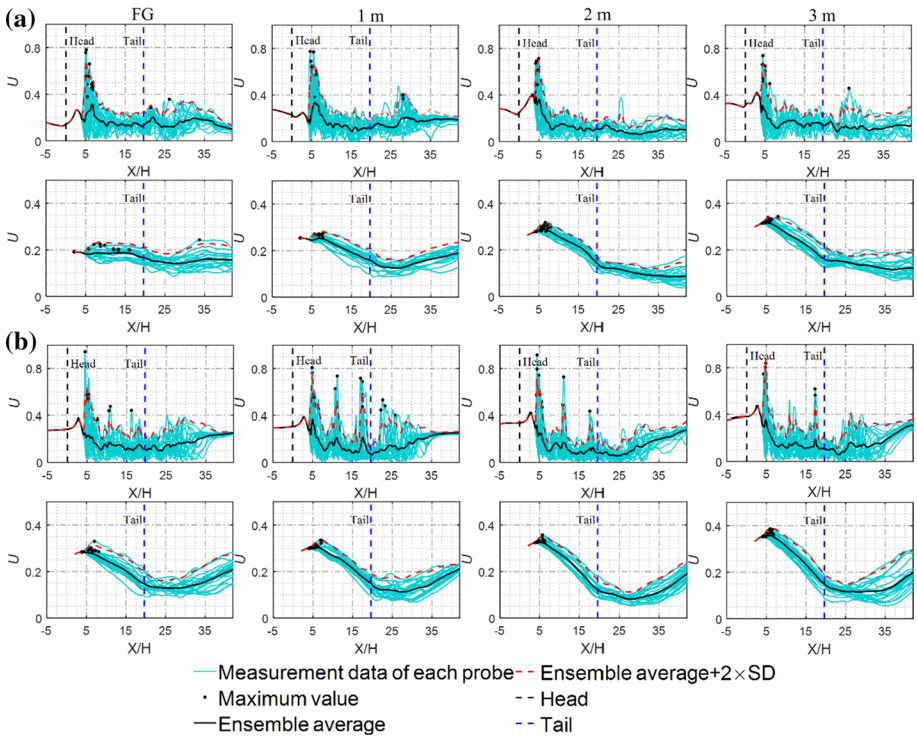


Fig. 11 Instantaneous U and 1 s MA for each probe: **a** track-side position and **b** platform position (top: raw data, bottom: 1 s MA). Blue line: measurement data for each probe. Black line: ensemble average. Red dashed line: ensemble average + $2 \times \text{SD}$. Black dotted line: maximum value. Black dashed line: the head of the train. Blue dashed line: the tail of the train

ensemble average of the raw data and 1 s MA increased by 31.2% and 64.6%, respectively, at $z=0.05H$, and the values increased by 27% and 26.1%, respectively, at $z=0.36 h$, as shown in Table 2. The standard deviation and the $U_{2\sigma}$ value with (TSI value) and without

Table 2 Characteristic velocity on the leeward side at the track-side and platform positions

	Without 1 s MA		With 1 s MA			
	\bar{U}_p	σ	$\bar{U}_p + 2\sigma$	\bar{U}_p	σ	$\bar{U}_p + 2\sigma$
$z=0.05H$						
FG	0.314	0.232	0.778	0.192	0.034	0.26
1 m	0.335	0.182	0.699	0.255	0.026	0.307
2 m	0.397	0.175	0.747	0.288	0.036	0.36
3 m	0.412	0.191	0.794	0.316	0.042	0.4
$z=0.36H$						
FG	0.367	0.199	0.765	0.284	0.041	0.366
1 m	0.386	0.199	0.784	0.304	0.035	0.374
2 m	0.415	0.206	0.827	0.326	0.031	0.388
3 m	0.466	0.256	0.978	0.358	0.057	0.472

1 s MA are also shown. The $U_{2\sigma}$ value with and without the 1 s MA increased with the increasing embankment height. The $U_{2\sigma}$ value without 1 s MA increased by 2.1% at $z=0.05H$ and by 27.8% at $z=0.36H$. The $U_{2\sigma}$ value of the 1 s MA increased by 53.8% at $z=0.05H$ and by 29% at $z=0.36H$. The increase of the embankment height had a significant impact on the TSI value on the leeward side.

3.3 Time-Averaged Flow Structure

3.3.1 Slipstream

Figure 12 shows the \bar{U} in the horizontal planes for the different embankment heights. Figures 12a and b correspond to 0.05 and 0.36H from the TOR, respectively. At both distances from the TOR, the variations in the embankment height had a minor impact on the WS of the train. However, due to the impact of the train, the \bar{U} values for different embankment heights were relatively small in the boundary layer region around the train on the WS. This is the reason for the rapid decrease of the \bar{U} value after the boundary layer region and its rapid increase in the near wake region in Fig. 9. The main differences in the \bar{U} values were around the train in the nose region A, tail region C, and LS region B, as illustrated in Fig. 12a. As shown in Fig. 12a and b, the strength of region A increased with the increasing embankment height. In the tail region C, at both distances from the TOR, the effect of the 1 m high embankment was stronger than those at the other embankment heights. This was the reason why the 1 m embankment height of the \bar{U} value in Fig. 10 was higher in the near wake region of the train. Variation in the distribution of the \bar{U} in the boundary layer region between different cases, was found to originate in the upstream flow in region A. As shown in Fig. 12b, the differences between cases were large in regions where the \bar{U} value was relatively small. Furthermore, there was a large \bar{U} value around the bogie, and it was very close to the car body, as shown in Fig. 12b. This was also the reason why there were some peaks in the boundary layer region at the measurement point 0.36H from the TOR and 0.51H from the COT, as shown in Fig. 10. However, no velocity peaks were observed at the measurement points far from the car body.

3.3.2 Streamlines

The slipstreams on the LS were correlated with the resulting flow structures. Figure 13 shows the streamlines of the time-averaged velocity projected on different planes at the cross-sections $x/L=0.03, 0.11, 0.21, 0.29, 0.43,$ and 0.57 from the nose tip for the four cases considered in this study. At $x/L=0.03$, the FG showed no vortex formation. The three cases with the embankment produced a vortex, V_{c1} , which detached from the LS of the embankment. The vortex for the 3 m embankment height was found to be strongest of the three cases. Another vortex V_{c2} , was found to detach from the lower A-pillars of the train nose on the upper part of the LS at $x/L=0.11$. The size of the vortex V_{c2} was found to increase with the increasing height of the embankment. For the FG, a vortex, V_{c2} , detached from the bottom of the train on the lower part of the LS, but the width was small. At location $x/L=0.43$, V_{c1} and V_{c2} disappeared, and the third vortex, V_{c3} . At the junction of the top and the leeward side of the train, a small vortex (dashed box) formed, due to the interaction between the incoming flow of the WS and the vortex V_{c3} . Similar flow picture was observed at $x/L=0.57$, where the most significant change was the width of the vortex V_{c3} and the distance from the center of the vortex V_{c3} to the COT. The widths of the vortex V_{c3}

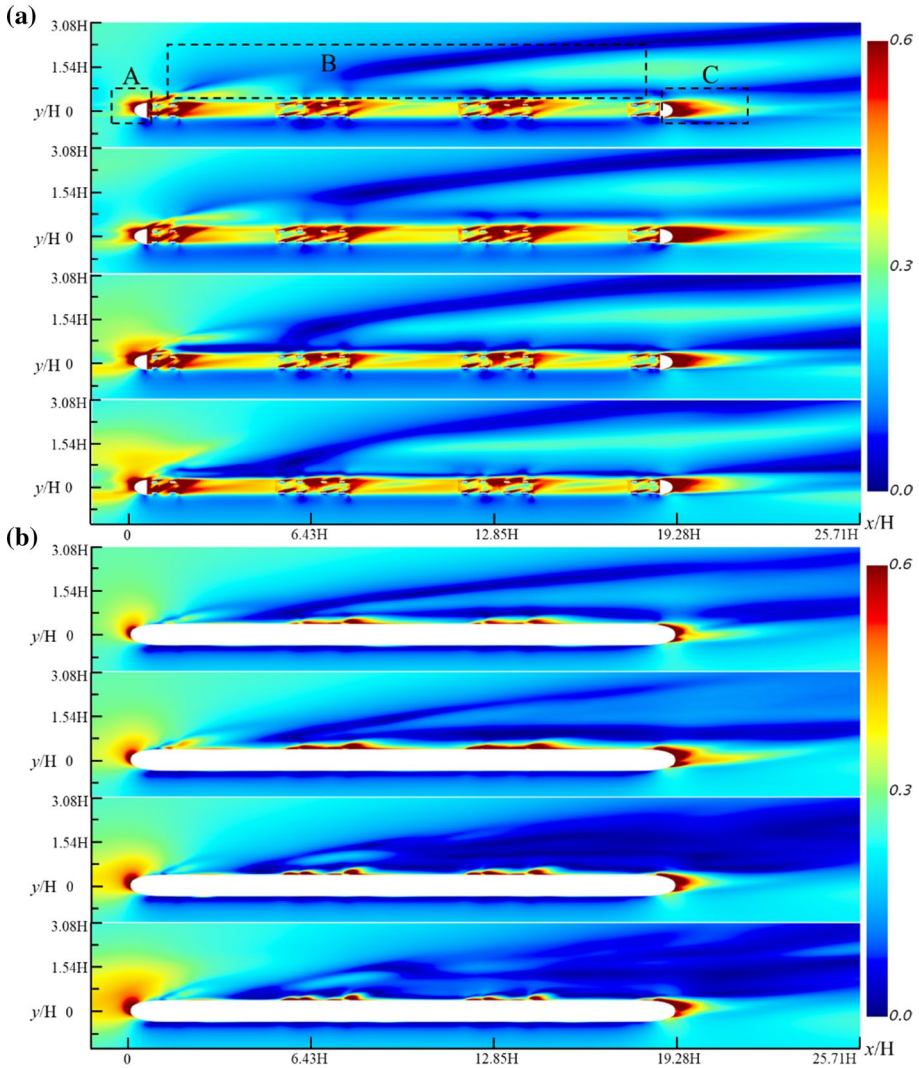


Fig. 12 Time-averaged U at different heights from the TOR: **a** $0.05H$ and **b** $0.36H$ (from top to bottom: FG, 1 m, 2 m, and 3 m)

in the spanwise direction were about $1.32H$, $1.65H$, $1.93H$, and $2.19H$ for the 0 m, 1 m, 2 m, and 3 m embankment heights, respectively. The center of the vortex V_{c3} was approximately $0.47H$ from the TOR and $1.1H$ from the COT for the FG, $0.41H$ from the TOR and $1.23H$ from the COT for the case with 1 m embankment height, $0.37H$ from the TOR and $1.25H$ from the COT for the case with 2 m embankment height, and $0.33H$ from the TOR and $1.42H$ from the COT for the case with 3 m embankment height.

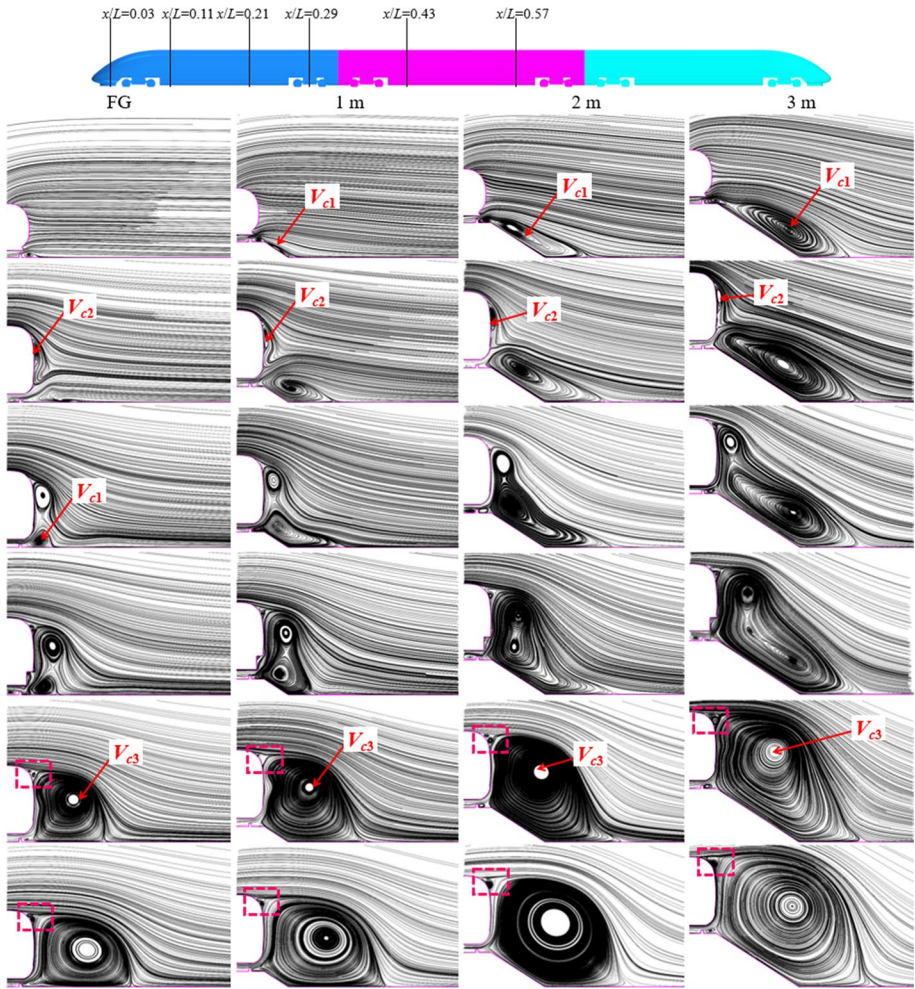


Fig. 13 Streamlines for the time-averaged velocity projected on the different planes (from left to right: FG, 1 m, 2 m, and 3 m; from top to bottom: $x/L=0.03, 0.11, 0.21, 0.29, 0.43,$ and 0.57)

3.4 Instantaneous flow structure

The second invariant of the velocity gradient, Q , is defined as

$$Q = \frac{1}{2} (\|\mathbf{\Omega}\|^2 - \|\mathbf{S}\|^2), \tag{4}$$

where $\mathbf{\Omega}$ is the rate-of-rotation tensor and \mathbf{S} is the rate-of-strain tensor. This quantity, often used to characterize the instantaneous flows around high-speed trains (Munoz-Paniagua et al. 2017; Hemida and Krajnović 2010; Chen et al. 2019b; Li et al. 2019) is presented in Fig. 14.

The turbulent fluctuations on the LS and the wake of the train in Fig. 14 were found to be large, with a complex flow. To facilitate the analysis, the vortex structure around

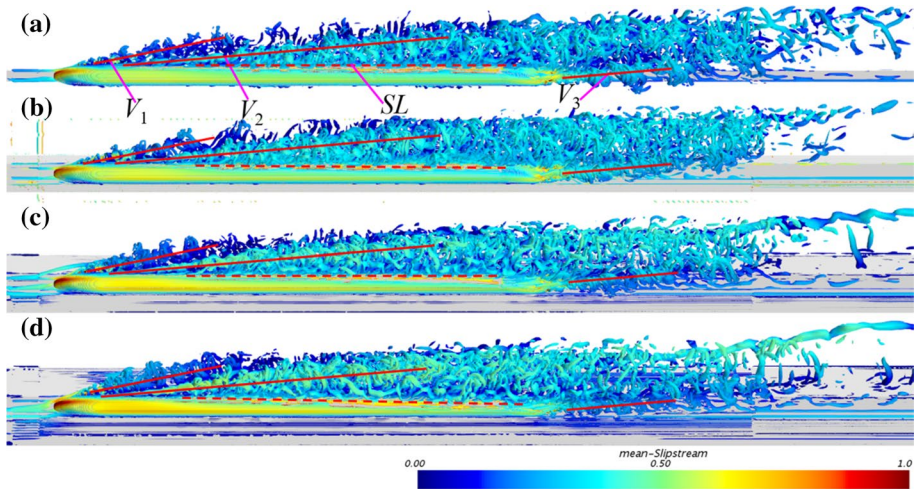


Fig. 14 Iso-surface of the instantaneous second invariant of the velocity gradient $Q = 20,000$ colored by the time-averaged slipstream velocity: **a** FG, **b** 1 m, **c** 2 m, and **d** 3 m

the train was divided into three parts based on the source: vortices V_1 , V_2 , and V_3 . The V_1 originates from the lower part of the head car nose and moves backward continuously from the beginning until it merges with vortex V_2 . The pulsation intensity of vortex V_1 was found to be different for different embankment heights. Figure 14a–d show that the intensity of vortex V_1 increases with the increasing embankment height. The vortex V_1 was found to have large influence on vortex V_2 . The boundary line of vortex V_2 , SL (red dashed line) was moved to the WS with the increase of the embankment height. Furthermore, the intensity of the vortex V_3 was found to decrease in strength with the increasing embankment height.

3.5 Aerodynamic force and moment

Figure 15 shows the time-averaged aerodynamic force and rolling moment coefficients, averaged over the time period between $154t^*$ and $617t^*$, for the different embankment heights. The aerodynamic force and rolling moment coefficients are calculated based on Eq. (2). The drag coefficients of the head, middle, and tail cars for different embankment heights, is shown in Fig. 15a. It can be seen that all values of drag coefficients increased with the increasing embankment height. When the embankment height increased from 0 to 3 m, the drag coefficients of the head, middle, and tail cars increased by 213.2%, 19.1%, and 15.3%, respectively. For the same embankment height, the drag coefficient of the tail car was the largest, and the drag coefficient of the head car was the smallest. Figure 15b shows the time-averaged side force coefficients of the head, middle, and tail cars for different embankment heights. Similarly as for the drag force, the side force coefficients increased continuously with the increasing embankment height. When the embankment height increased from 0 to 3 m, the side force coefficients of the head, middle, and tail cars increased by 27.4%, 22.5%, and 251%, respectively. Figure 15c shows the lift force coefficients of the head, middle, and tail cars for different embankment heights. With the increasing embankment height, the lift force coefficients of the head and middle cars increased continuously, and the lift force coefficient of the tail car decreased. When the

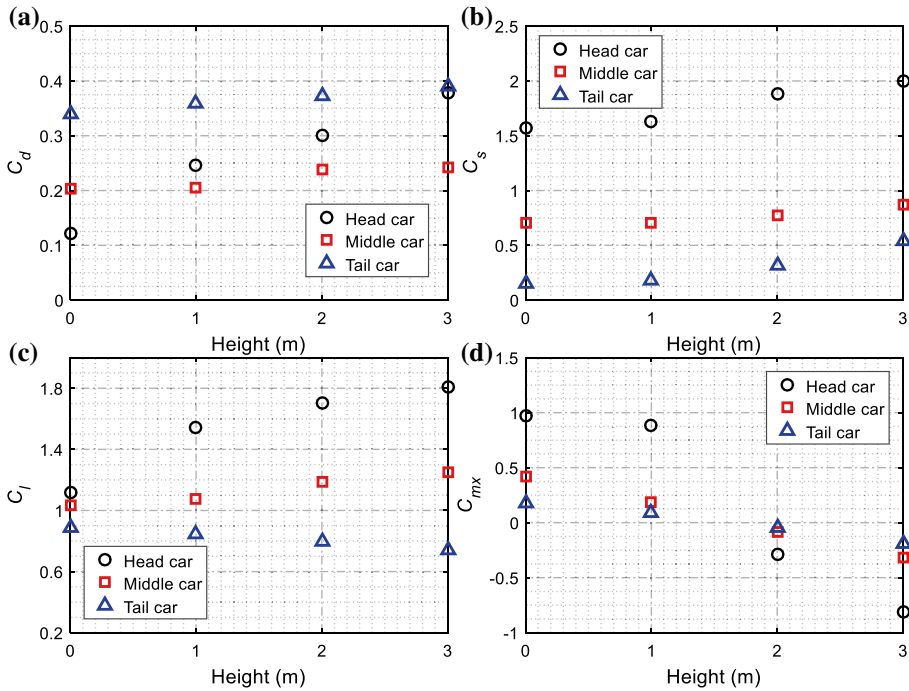


Fig. 15 Time-averaged aerodynamic force and moment coefficients: **a** drag coefficients, **b** side force coefficients, **c** lift force coefficients, and **d** rolling moment coefficients

embankment height increased from 0 to 3 m, the lift force coefficient of the head and middle cars increased by 62.1% and 21.2%, respectively, and the lift force coefficient of the tail car decreased by 16.3%. Figure 15d shows the rolling moment coefficients of the head, middle, and tail cars for different embankment heights. The rolling moment center was in the leeward rail. When the train moved over the FG, the rolling moment rotated in the leeward side of the train. Due to the speed-up effect of the embankment, the upstream flow accelerated and it ended up on the leeward side of the train after its passage through the bottom of the train, thereby reducing the rolling moment of the train. With the increase of the embankment height, the speed-up effect was found to be more significant, causing the reversed rotation direction of the rolling moment. In summary, changing the embankment height had a significant influence on the aerodynamic forces and the moment of the train.

4 Conclusions

The study presents a numerical investigation of the flow around a high-speed train at embankments of various heights. The simulation technique was and the quantities studied are the aerodynamic forces and the slipstream velocities. Both the time-averaged and the instantaneous aerodynamic properties as well as the underlying flow mechanisms were studied. The results of the study can be summarized as follows:

1. The variation in the embankment height was found to have a small effect on the time-averaged slipstream velocity on the windward side of the train. The opposite was the case on the leeward side of the train, with a peak value at the slipstream in the nose region of the train. With the increase in the embankment height, the TSI values increased continuously at the distances $0.77H$ from the COT, $0.05H$ from the TOR and $0.77H$ from the COT, $0.36H$ from the TOR. When the embankment height increased from 0 to 3 m, the TSI value increased by 53.8% at the distances $0.77H$ from the COT, $0.05H$ from the TOR and 29% at the distances $0.77H$ from the COT, $0.36H$ from the TOR.
2. The variation in the embankment height was found to have a significant influence on the formation and development of the main vortices on the leeward side of the train. Furthermore, the change in the embankment height, resulted in the change of the position of the separation line (*SL*) at the top of the train. For the embankment height of 1 m, the *SL* was found to be closest to the windward side of the train. In the instantaneous flow field, two main vortices were identified on the leeward side of the train. With the increase in the embankment height, the strength of the lower vortex was found to increase. The two vortices merged in a single in the middle region of the train.
3. The aerodynamic forces and the rolling moments of trains for different embankment heights were significantly different. The drag and side forces increased continuously with the increasing embankment height. The lift forces of the head and middle cars increased continuously with the increasing embankment height, while the lift force of the tail car decreased. Once the embankment height was exceeded 2 m, the rolling moment was found to change its direction.

Acknowledgements This work was supported by the National Key R&D Program of China (2016YFB1200601-B14).

Compliance with Ethical Standards

Conflict of interest The authors declare that they have no conflict of interest.

References

- Baker, C.J.: The flow around high speed trains. *J. Wind Eng. Ind. Aerodyn.* **98**(6–7), 277–298 (2010)
- Baker, C.J., Quinn, A., Sima, M., Hoefener, L., Licciardello, R.: Full-scale measurement and analysis of train slipstreams and wakes. Part 1: ensemble averages. *Proc. Inst. Mech. Eng. Part F J. Rail Rapid Transp.* **228**(5), 451–467 (2014a)
- Baker, C.J., Quinn, A., Sima, M., Hoefener, L., Licciardello, R.: Full-scale measurement and analysis of train slipstreams and wakes. Part 2: Gust analysis. *Proc. Inst. Mech. Eng. Part F J. Rail Rapid Transp.* **228**(5), 468–480 (2014b)
- Bell, J.R., Burton, D., Thompson, M., Herbst, A., Sheridan, J.: Wind tunnel analysis of the slipstream and wake of a high-speed train. *J. Wind Eng. Ind. Aerodyn.* **134**, 122–138 (2014)
- Bell, J.R., Burton, D., Thompson, M.C., Herbst, A.H., Sheridan, J.: Flow topology and unsteady features of the wake of a generic high-speed train. *J. Fluids Struct.* **61**, 168–183 (2016)
- Bell, J.R., Burton, D., Thompson, M.C., Herbst, A.H., Sheridan, J.: The effect of tail geometry on the slipstream and unsteady wake structure of high-speed trains. *Exp. Therm. Fluid Sci.* **83**, 215–230 (2017)
- Bocciolone, M., Cheli, F., Corradi, R., Muggiasca, S., Tomasini, G.: Crosswind action on rail vehicles: wind tunnel experimental analyses. *J. Wind Eng. Ind. Aerodyn.* **96**(5), 584–610 (2018)
- CEN European Standard: Railway Applications–Aerodynamics. Part 6: Requirements and Test Procedures for Cross Wind Assessment, CEN EN 14067–6 (2018)
- Cheli, F., Ripamonti, F., Rocchi, D., Tomasini, G.: Aerodynamic behaviour investigation of the new EMUV250 train to cross wind. *J. Wind Eng. Ind. Aerodyn.* **98**(4–5), 189–201 (2010a)
- Cheli, F., Corradi, R., Rocchi, D., Tomasini, G., Maestrini, E.: Wind tunnel tests on train scale models to investigate the effect of infrastructure scenario. *J. Wind Eng. Ind. Aerodyn.* **98**(6–7), 353–362 (2010b)

- Chen, Z.W., Liu, T.H., Yan, C.G., Yu, M., Guo, Z.J., Wang, T.T.: Numerical simulation and comparison of the slipstreams of trains with different nose lengths under crosswind. *J. Wind Eng. Ind. Aerodyn.* **190**, 256–272 (2019a)
- Chen, G., Li, X.B., Liu, Z., Zhou, D., Wang, Z., Liang, X.F., Krajnović, S.: Dynamic analysis of the effect of nose length on train aerodynamic performance. *J. Wind Eng. Ind. Aerodyn.* **184**, 198–208 (2019b)
- Diedrichs, B., Sima, M., Orellano, A., Tengstrand, H.: Crosswind stability of a high-speed train on a high embankment. *Proc. Inst. Mech. Eng. Part F J. Rail Rapid Transp.* **221** (2), 205–225: (2007)
- DIN Standards Committee: *Railway/Normenausschuss Fahrweg und Schienenfahrzeuge (FSF)* (2018)
- European Union Agency for Railways: Commission Regulation (EU) No 1302/2014 concerning a technical specification for interoperability relating to the ‘rolling stock—locomotives and passenger rolling stock’ subsystem of the rail system (2014)
- Flynn, D., Hemida, H., Soper, D., Baker, C.: Detached-eddy simulation of the slipstream of an operational freight train. *J. Wind Eng. Ind. Aerodyn.* **132**, 1–12 (2014)
- Flynn, D., Hemida, H., Baker, C.: On the effect of crosswinds on the slipstream of a freight train and associated effects. *J. Wind Eng. Ind. Aerodyn.* **156**, 14–28 (2016)
- Guo, Z.J., Liu, T.H., Chen, Z.W., Liu, Z., Monzer, A., Sheridan, J.: Study of the flow around railway embankment of different heights with and without trains. *J. Wind Eng. Ind. Aerodyn.* **202**, 104203 (2020)
- Hemida, H., Krajnović, S.: LES study of the influence of the nose shape and yaw angles on flow structures around trains. *J. Wind Eng. Ind. Aerodyn.* **98**(1), 34–46 (2010)
- Krajnović, S., Ringqvist, P., Nakade, K., Basara, B.: Large eddy simulation of the flow around a simplified train moving through a crosswind flow. *J. Wind Eng. Ind. Aerodyn.* **110**, 86–99 (2012)
- Li, X.L., Chen, G., Zhou, D., Chen, Z.W.: Impact of different nose lengths on flow-field structure around a high-speed train. *Appl. Sci. Basel* **9**(21), 4573 (2019)
- Luckhurst, S., Varney, M., Xia, H., Passmore, M.A., Gaylard, A.: Computational investigation into the sensitivity of a simplified vehicle wake to small base geometry changes. *J. Wind Eng. Ind. Aerodyn.* **185**, 1–15 (2019)
- Morden, J.A.: *A Numerical Investigation of the Effects of Crosswinds Upon the Aerodynamic Characteristics of a High-Speed Passenger Train and Its Slipstream* (Ph.D. thesis). The University of Birmingham (2016)
- Muld, T.W., Efraimsson, G., Henningson, D.S.: Flow structures around a high-speed train extracted using proper orthogonal decomposition and dynamic mode decomposition. *Comput. Fluids* **57**, 87–97 (2012)
- Munoz-Paniagua, J., García, J., Lehueur, B.: Evaluation of RANS, SAS and IDDES models for the simulation of the flow around a high-speed train subjected to crosswind. *J. Wind Eng. Ind. Aerodyn.* **171**, 50–66 (2017)
- Noguchi, Y., Suzuki, M., Baker, C.J., Nakade, K.: Numerical and experimental study on the aerodynamic force coefficients of railway vehicles on an embankment in crosswind. *J. Wind Eng. Ind. Aerodyn.* **184**, 90–105 (2019)
- Pope, C.: *Safety of Slipstreams Effects Produced by Trains*. A Report Prepared by Mott MacDonald Ltd. for Railway Safety and Standards Board, 2 edn. Mott MacDonald, Croydon (2006)
- Schober, M., Weise, M., Orellano, A., Deeg, P., Wetzel, W.: Wind tunnel investigation of an ICE 3 end car on three standard ground scenarios. *J. Wind Eng. Ind. Aerodyn.* **98**(6–7), 345–352 (2010)
- Shur, M.L., Spalart, P.R., Strelets, M.K., Travin, A.K.: A hybrid RANS–LES approach with delayed-DES and wall-modelled les capabilities. *Int. J. Heat Fluid Flow* **29**(6), 1638–1649 (2008)
- Suzuki, M., Tanemoto, K., Maeda, T.: Aerodynamic characteristics of train/vehicles under cross winds. *J. Wind Eng. Ind. Aerodyn.* **91**, 209–218 (2003)
- Tomasini, G., Giappino, S., Corradi, R.: Experimental investigation of the effects of embankment scenario on railway vehicle aerodynamic coefficients. *J. Wind Eng. Ind. Aerodyn.* **131**, 59–71 (2014)
- Wang, S.B., Bell, J.R., Burton, D., Herbst, A.H., Sheridan, J., Thompson, M.C.: The performance of different turbulence models (URANS, SAS and DES) for predicting high-speed train slipstream. *J. Wind Eng. Ind. Aerodyn.* **165**, 46–57 (2017)
- Wang, S.B., Burton, D., Herbst, A.H., Sheridan, J., Thompson, M.C.: The effect of bogies on high-speed train slipstream and wake. *J. Fluids Struct.* **83**, 471–489 (2018a)
- Wang, S.B., Burton, D., Herbst, A.H., Sheridan, J., Thompson, M.C.: The effect of the ground condition on high-speed train slipstream. *J. Wind Eng. Ind. Aerodyn.* **172**, 230–243 (2018b)
- Xia, C., Wang, H., Shan, X., Yang, Z., Li, Q.: Effects of ground configurations on the slipstream and near wake of a high-speed train. *J. Wind Eng. Ind. Aerodyn.* **168**, 177–189 (2017)
- Zhang, J., Wang, J., Tan, X.M., Gao, G.J., Xiong, X.: Detached eddy simulation of flow characteristics around railway embankments and the layout of anemometers. *J. Wind Eng. Ind. Aerodyn.* **193**, 103968 (2019)